Petroleum Science xxx (xxxx) xxx

Contents lists available at ScienceDirect

Petroleum Science

journal homepage: www.keaipublishing.com/en/journals/petroleum-science

Original Paper

Evolution of pore systems in low-maturity oil shales during thermal upgrading —Quantified by dynamic SEM and machine learning

Jun Liu [a, *], Xue Bai [b, c, **], Derek Elsworth [d]

[a] Key Laboratory of Deep Underground Science and Engineering (Ministry of Education), Institute of New Energy and Low-Carbon Technology, Sichuan University, Chengdu, 610065, Sichuan, China
[b] International Quantum Academy, Shenzhen, 518048, Guangdong, China
[c] Shenzhen Institute of Advanced Electronic Materials, Shenzhen Institute of Advanced Technology, Chinese Academy of Sciences, Shenzhen, 518055, Guangdong, China
[d] Department of Energy and Mineral Engineering, Pennsylvania State University, University Park, PA 16802, USA

ARTICLE INFO

Article history:
Received 18 September 2023
Received in revised form
26 December 2023
Accepted 27 December 2023
Available online xxx

Edited by Yan-Hua Sun

Keywords:
Low-maturity oil shale
Pore elongation
Organic matter pyrolysis
In-situ thermal upgrading
Scanning electron microscopy (SEM)
Machine learning

ABSTRACT

In-situ upgrading by heating is feasible for low-maturity shale oil, where the pore space dynamically evolves. We characterize this response for a heated substrate concurrently imaged by SEM. We systematically follow the evolution of pore quantity, size (length, width and cross-sectional area), orientation, shape (aspect ratio, roundness and solidity) and their anisotropy —interpreted by machine learning. Results indicate that heating generates new pores in both organic matter and inorganic minerals. However, the newly formed pores are smaller than the original pores and thus reduce average lengths and widths of the bedding-parallel pore system. Conversely, the average pore lengths and widths are increased in the bedding-perpendicular direction. Besides, heating increases the cross-sectional area of pores in low-maturity oil shales, where this growth tendency fluctuates at < 300 °C but becomes steady at > 300 °C. In addition, the orientation and shape of the newly-formed heating-induced pores follow the habit of the original pores and follow the initial probability distributions of pore orientation and shape. Herein, limited anisotropy is detected in pore direction and shape, indicating similar modes of evolution both bedding-parallel and bedding-normal. We propose a straightforward but robust model to describe evolution of pore system in low-maturity oil shales during heating.

1. Introduction

The worldwide shale oil-equivalent reserve is approximately three times that of crude oil at 690 × 10^9 t (Zhou et al., 2018). This huge potential represents a promising energy alternative in energy supply (Feng et al., 2020; Liu et al., 2020; Altawati et al., 2021; Lin et al., 2021; Bolotov et al., 2023). Moreover, the rapid development of shale oil plays a significant factor impacting the pricing and availability of global oil supplies. For example, plentiful shale oil arguably provided the impetus for repealing the 1975 United States ban on crude oil exports in December 2015 that enabled the US to become a net oil exporter in October 2019, however briefly (Vatter et al., 2022).

Although the utilization of shale oil is strategically important, its recovery remains challenging due to the nature of the ultra-low permeability reservoirs (Feng et al., 2020; Wu et al., 2021; Xu et al., 2022). No universal methodology for shale oil extraction is applicable to all reservoirs. For example, hydraulic fracturing has been successfully applied to recover product from Eagle Ford shale formations (Chaudhary et al., 2011), while CO_2 huff-n-puff is useful in the oil production from Bakken shale formation (Alfarge et al., 2017). *In-situ* heating is another technique used to upgrade especially low-maturity oil shales using temperatures of the order of ~300–500 °C to increase oil yield through pyrolysis used worldwide (Sadiki et al., 2003; Wang et al., 2020; Comincioli et al., 2021; Jin et al., 2021; Yang et al., 2021; He et al., 2022; Vatter et al., 2022).

For *in-situ* heating accommodating pyrolysis, the high thermal loads inevitably transform the pore system (Wang et al., 2010; Li et al., 2020a, 2020b; Yu et al., 2020; He et al., 2022). This is

* Corresponding author.
** Corresponding author. International Quantum Academy, Shenzhen, 518048, Guangdong, China.
E-mail addresses: j.liu@scu.edu.cn (J. Liu), baixue@iqasz.cn (X. Bai).

https://doi.org/10.1016/j.petsci.2023.12.021

important since the connectivity determines migration in tight shales and thus the precise characteristics of the high temperature alteration of the pore system is important in defining the effectiveness of *in-situ* thermal upgrading. Numerous studies have explored this aspect (Li et al., 2020a, 2020b; Zhou et al., 2021; Zhao et al., 2022). Microwave heating with graphite powder to enable heating to 900 °C (Wang et al., 2010) showed significant influence on the specific surface area and specific pore volume, as well as mesopore development. Micro-CT imaging has measured pore and fracture evolution at high temperature (up to 600 °C) for oil shales from the Daqing and Yan'an areas, China (Zhao et al., 2012). These have defined three evolutionary stages of the pore structure during the thermal process (up to 550 °C) relating to different degrees of maturity; a complex development stage, a massive development stage and a uniform development stage, detected and differentiated using CO_2/N_2 adsorption (Tan et al., 2021). This understanding in characterizing pore structure variation during heating is remarkable and strategically important in enhancing our understanding of *in-situ* heating operations for shale oil development (Geng et al., 2017; Shi et al., 2017; Zhu et al., 2018; He et al., 2022; Luo et al., 2023).

However, current laboratory evaluations remain imprecise since many are completed after cooling, rather than evaluated at elevated and sustained temperatures (Zhao et al., 2012; Luo et al., 2023). This deficiency leaves the results as equivocal, since the cooling process results in at least two important phenomena: 1) cooling shrinkage and thermal fracturing of the shale matrix/pores and 2) solidification of hydrocarbon fluids that are previously mobile at high temperature. In addition, investigations into cooled specimens are incapable of following the continuous evolution in the shale pore system during upgrading by cycled *in-situ* heating. Such evolutionary changes in pore structure are crucial in defining complex couple process interactions at high temperature with *in-situ* studies needed for improved clarification of potential benefits during upgrading.

This work makes direct observations and real-time characterization of the pore system that evolves in low-maturity oil shales during thermal upgrading. We use scanning electron microscopy (SEM) for a sample on an *in-situ* heated substrate capable of temperatures to 500 °C. For the first time we define key parameters defining the thermal response. These key quantitative parameters include the number (N), length (L), width (W), cross-sectional area (S), orientation (θ), aspect ratio (AR), roundness and solidity, obtained by machine learning. In particular, these changes are defined on a single and constant region captured by SEM during the gradual rise in temperature. Moreover, in this work, the anisotropic properties are explored by observing in orthogonal sections both parallel and perpendicular to bedding. Accordingly, this work presents direct visualization and quantitative determination on how high temperatures impact the evolution of the pore system of oil shales —ultimately instructive in understanding the impacts of *in-situ* heating-related low-maturity oil shale upgrading.

2. Materials and methodologies

We introduce the methods of sample collection and preparation together with a description of the heads SEM stage for imaging and the methods used to characterize the pore system.

2.1. Sampling preparation and experimental scheme

Oil shale samples were cored from the Upper Cretaceous Qingshankou Formation at a depth of about 1100 m. This well pierces the continental retro-arc Songliao Basin, NE China. This basin is a typical Mesozoic basin superimposed on Palaeozoic basement (Xu et al., 2015) containing several sets of oil-bearing formations, of which the Qingshankou Formation is a promising low-maturity shale reservoir (Liu et al., 2020; Lin et al., 2021; He et al., 2022). The core returns a vitrinite reflectance (R_o) value of 0.95% (low-maturity) and a total organic carbon content (TOC) of 4.8%. Three samples were prepared for the investigation (H1, H2 and V1) (Fig. 1(a)). The samples H1 and H2 are cut bedding-plane parallel and V1 bedding-pane perpendicular. The three SEM samples are approximately the same sizes, 3−4 mm in length (l), 2−3 mm in width (w), and 0.5 mm in thickness (d) (Fig. 1(b)).

The samples are placed in an Apreo 2S SEM (Thermo Scientific). All three samples are exposed to incremented temperatures of 25, 100, 200, 300, 400, and 500 °C (Fig. 1(c)). During the heating process, the temperature rise rate is set as 5 °C/min, this low heating rate avoids any thermal shock induced to the pore system and enables the maturity increase of organic matter in the involved oil shale samples (Sweeney and Burnham, 1990). At each temperature, the operating temperature is maintained for 2 h to allow sufficient pyrolysis of the organic matter, followed by SEM imaging of the fixed view (Fig. 1(c)). Before terminating the experiment, all samples were cooled to 25 from 500 °C (and kept for 2 h) to investigate whether the cooling process has additional influence on the pore system. Correspondingly, the temperature is decremented slowly at 5 °C/min to prevent reverse alterations resulting from a sudden drop in temperature. The fixed imaged window for bedding-parallel sample H1 is shown in Fig. 1(d) and measured as ~1212 μm^2, and that for sample H2 and bedding-perpendicular sample V1 is similar (~1742 μm^2) (Fig. 1(e) and (f)). In this work, the applicability of the 2-h exposure time at each temperature is justified based on the observations of Zhao et al. (2012) and Luo et al. (2023).

2.2. Experimental setup and approach

We present the details of the SEM used for imaging and introduce the machine learning methods used to recover the pore parameters. We use these parameters to quantify how the pore system evolves.

2.2.1. SEM apparatus with in-situ heating stage

We image the morphological evolution of low-maturity oil shales during heating as described in Fig. 1(c) using field-emission SEM equipped with a unique *in-situ* heating stage. A water chiller is connected to the SEM chamber (Fig. 2(a)) to facilitate temperature control of the heating stage. The stage is present in a high vacuum environment (i.e., 3×10^{-3} Pa) (Fig. 2(b)) during the measurement to prevent oxidation of the organic matter. Heater tape sets the approximate desired temperature with circulating water pipes connected to the chiller providing precise temperature control (Fig. 2(b)). In addition, a heat shield is set to prevent fugitive emissions (electrons) on the detector and to thus enhance the quality of the imaging at elevated temperatures. During the measurement, the sample is placed on the silicon heating substrate and is fastened by screw and press clamps (Fig. 2(c)). A high-precision temperature sensor is mounted below the substrate to monitor the temperature in real-time.

2.2.2. Pore system recognition

The SEM captures are fed into ImageJ with a trainable Weka segmentation (TWS) plugin to quantify the morphology of the pore system. This plugin works as a bridge between the image processing fields and the machine learning to produce image segmentation based on pixel classification. This workflow is described in Fig. 3(a). First, the SEM capture is opened by ImageJ and then the pixel-based machine learning is conducted by the TWS plugin to

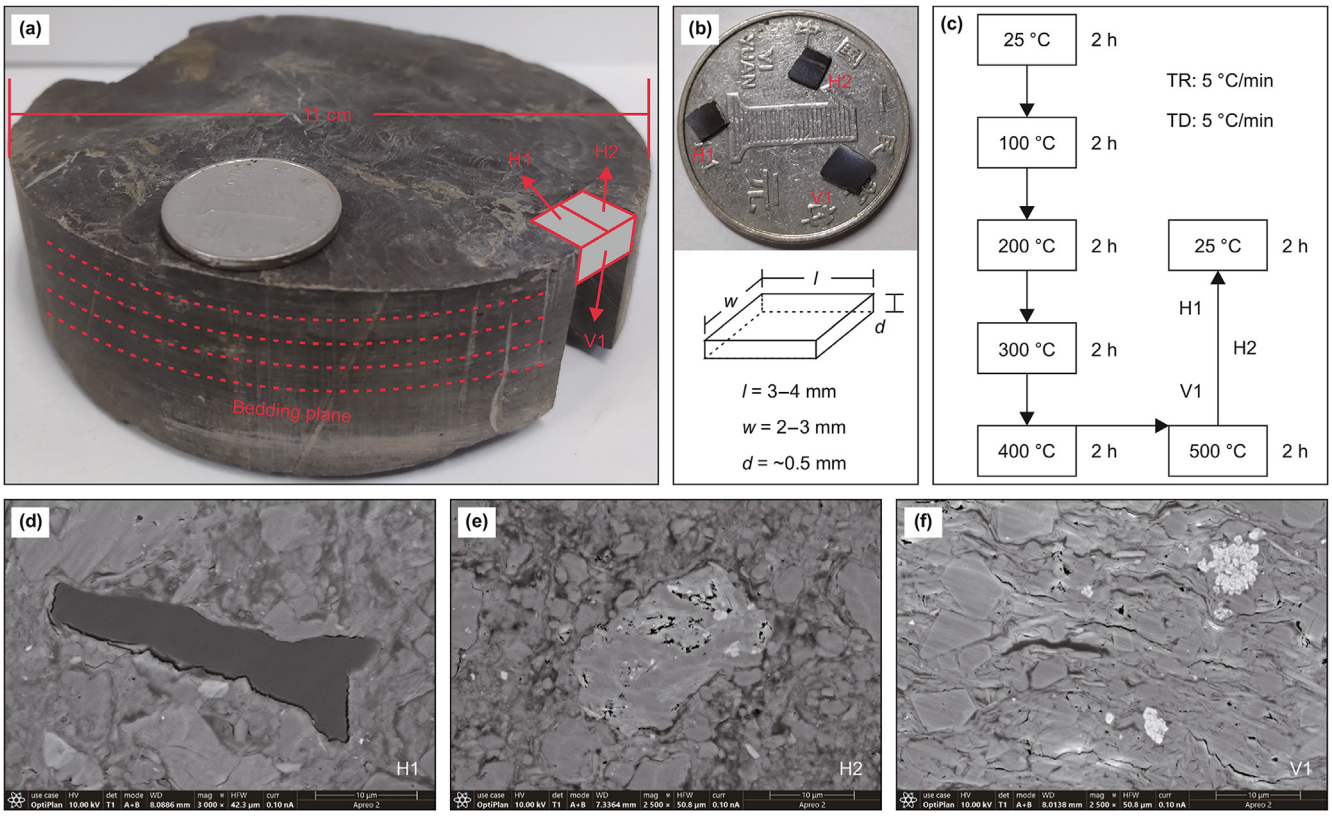

Fig. 1. Sample preparation and basic procedures for measurements. (**a**) Oil shale core; (**b**) Samples for SEM observations; (**c**) Temperature cycling during SEM measurement; Selected views during SEM observation for samples H1 (**d**), H2 (**e**), and V1 (**f**) before heating. TR and TD represent the rate for temperature rise and temperature reduction, respectively.

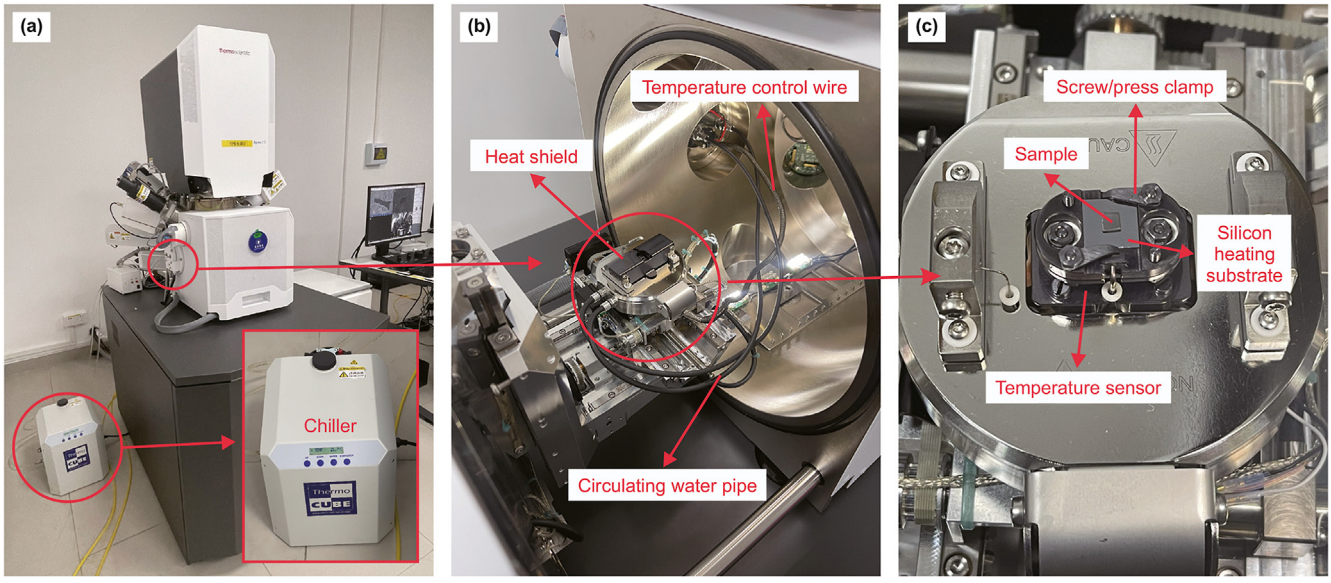

Fig. 2. SEM apparatus with fabricated *in-situ* heating stage. (**a**) SEM profile and water chiller; (**b**) *In-situ* heating stage; (**c**) Sample substrate.

distinguish pore space and other background in the SEM scene. Secondly, suitable training features from the Weka segmentation are defined to acquire the pore system in SEM image. Then, the acquired pores are marked on the original input SEM capture to calibrate the pore information, while more training is applied if the former pore recognition is unsatisfactory. Following this, the acquired pore system is confirmed and supports the automatic measurement for pore parameters (like *L* and *W*) depending on the built-in program in ImageJ (Fig. 3(b)). Meanwhile, the SEM image binary, where any pixel is either 0 (black) or 255 (white), is also output for confirmatory checking of the pore structure in selected samples (Fig. 3(a)). Through this workflow, the pore system is

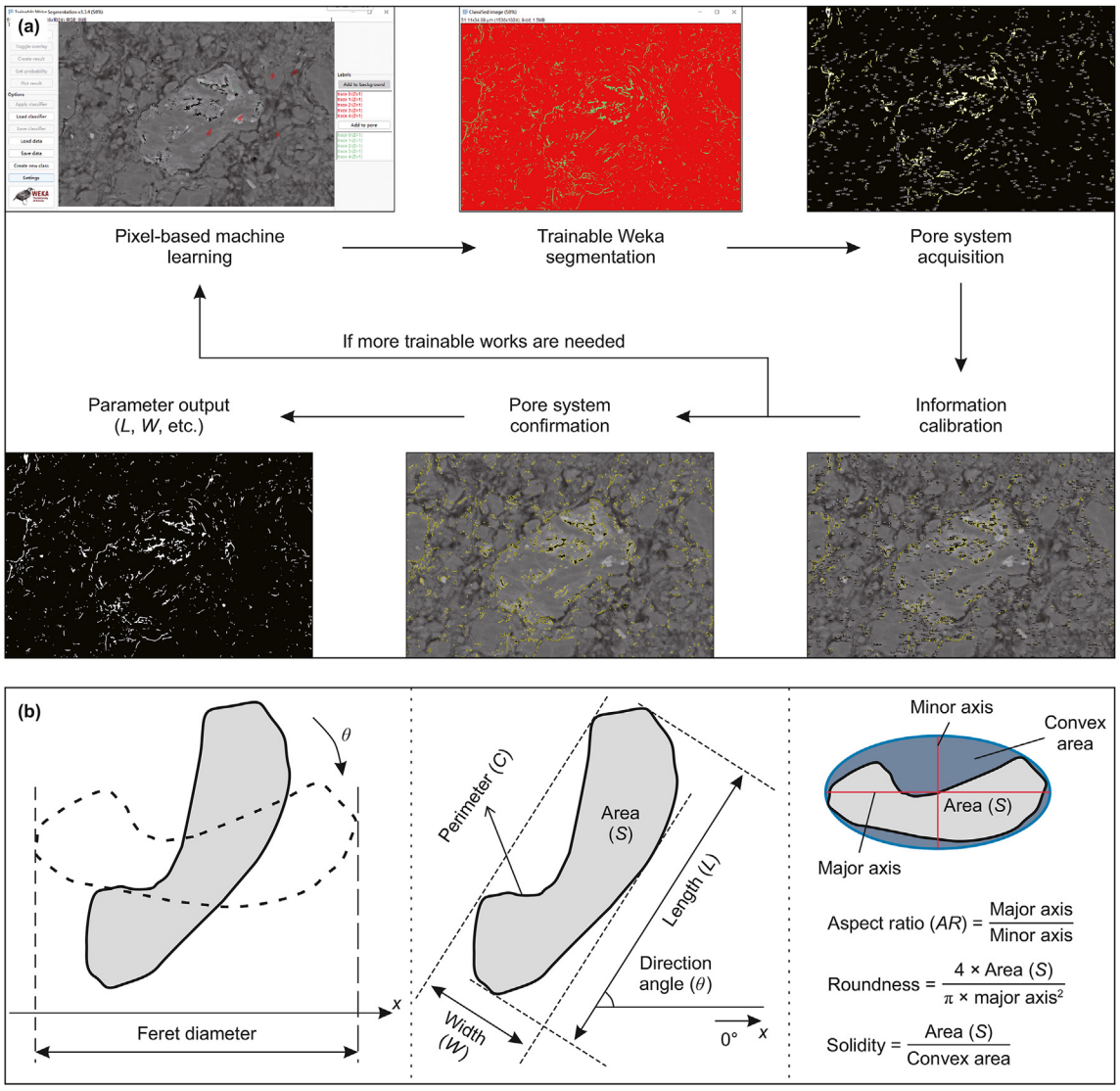

Fig. 3. Pore system measurement. (**a**) Flow diagram for pore system acquisition using the TWS plugin in ImageJ software; (**b**) Definition of output parameters for pore system.

transformed from a visual map (SEM image) to a quantitative structured system (pore parameters) with workflow confirmed by others (Arganda-Carreras et al., 2017; Lormand et al., 2018).

2.2.3. Quantitative description of pore system

The automated pore recognition system is applied to the SEM images and defines the parameter *N* representing the pore number. In addition, the Feret diameter is acquired from calculating the length of pore projection at a specified angle to the unit on the *x*-axis (horizontal direction) for adopting the parameters *L* and *W* (Soroushian and Elzafraney, 2005; Sezer et al., 2008; Liu et al., 2011). Therein, *L* and *W* denote the maximum and minimum values of the Feret diameter, respectively (Fig. 3(b)). The specific angle when measuring the maximum Feret diameter (i.e., *L*) is defined as the parameter θ, which varies from 0° to 180° and is an indicator of the directionality (orientation) of pores in the SEM image. Furthermore, the parameter *S* represents the pore area and is defined by the number of pixels filling a pore (Fig. 3(b)).

We also measure the *AR*, roundness and solidity from ImageJ. Fig. 3(b) defines their basic form and calculation. In this work, the parameters *AR*, roundness and solidity are introduced to enhance the description of elongation and overall shape of the pore structure, with their physical significance presented more thoroughly by Pavicic et al. (2021).

3. Results and discussion

We use the machine learning outputs of the pore information from the SEM images to investigate the evolution of the number, size, orientation and shape of pores in low-maturity oil shales and their anisotropy during thermal upgrading. We explore mechanisms responsible for this evolutions and additional prospects for future research defined.

3.1. Pore number description

We define the number of acquired pores, *N*, in Fig. 4. Prior to heating (i.e., at 25 °C), sample V1 has more concentrated pores, with ~0.5 pores per square micron, than the other two samples. This observation partly supports the universal presence of anisotropic permeability in shales with bedding-plane-parallel permeability usually greater than that perpendicular to bedding (Liu et al.,

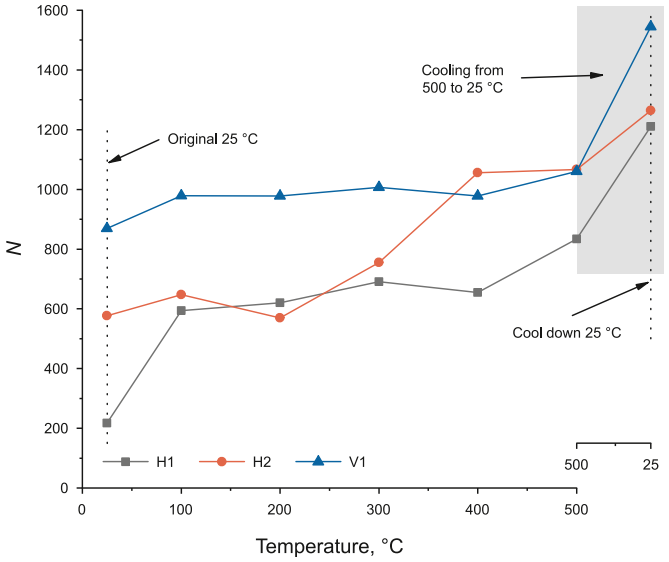

Fig. 4. Number evolution of acquired pores in SEM captures of low-maturity oil shales. *N* represents the number of acquired pores.

2021). As the temperature increased, the overall number of pores in the low-maturity shale increased. With thermal loading, some new pores formed (Fig. 5(a)), which increased *N*; however, some originally plugged (or disconnected) pores became connected (Fig. 5(b)), thus lowering *N*. As a result, this increase and decrease in the number of pores jointly affected the *N* value under increasing temperature. The newly formed pores were mostly in contact with organic matter (Fig. 5(a)–(d)) and partially correlated with inorganic minerals (Fig. 5(d)). In addition, for samples H1 and V1, the simultaneous increases and decreases in *N* caused a slight net increase in the number of pores, *N*, as shown in Fig. 5(c). Nevertheless, sample H2 experienced a relatively rapid growth in *N* (Fig. 4), apparent in the abundance of newly formed pores in the SEM image in Fig. 5(d). In general, the pore system in the low-maturity oil shale became more developed as a result of thermal upgrading, supported by the pore space that was newly formed or/and newly connected.

In addition, the number of pores, *N*, further increased as a result of cooling from 500 to 25 °C and for all samples. Apparent in the SEM images, some pores were extended (Fig. 5(e)) or newly formed (Fig. 5(f)), indicating that the pore structure was also impacted by the thermal stress reversal during cooling. The differential shrinkage of the shale matrix (due to contrasting mineral grains) induced by cooling potentially developed newly formed pores at the edge of the mineral grains (Fig. 5(f)) where differential thermal expansion may be the cause; however, more observations are needed to clarify this deduction. Nevertheless, the pore structure did evolve during cooling, emphasizing the need to observer response in both heating and cooling, as the peak-heated condition is not necessarily represented in the cooled sample.

3.2. Pore size evolution

Outputs of pore length, *L*, width, *W*, and area, *S*, provide a quantitative basis for evaluating the evolution characteristics of the pore network at different temperatures during the heating and cooling processes.

3.2.1. Pore lengths L and widths W

The *L* value expresses the change in length of pores during the heating and thermal loading process. For samples H1 and H2, the high temperature has a tendency to minimize the overall *L* values (Fig. 6(a)). Note that although the variation in the average *L* of sample H2 is less evident, its median follows a similar variation pattern with that of sample H1 (Fig. 6(b)). This result shows that the evolution of the pore space deceases the average pore size with increasing temperature, for the bedding-parallel samples. This occurs mainly because the newly formed pores (e.g., from the pyrolysis of organic matter) are small (Fig. 5). In contrast, the average *L* value for sample V1 shows a slight upward trend (Fig. 6(c)), in contrast to the results from samples H1 and H2, where anisotropic properties are apparent. Primarily, the pore widths (*W*) vary similarly to the trends in the *L* values, in which the newly formed pores are likely to lower the average *W* for the H1 and H2 samples, similarly showing the presence of anisotropy (Fig. 6(d)–(f)).

The evolution of pore sizes during heating is defined by multiple interacting factors that are simultaneously activated. First, newly formed pores are initially small, and this behavior lowers the average *L* or/and *W* values. However, some original plugged/disconnected pores become connected, and some pores become extended, as shown in Fig. 5 —this increases the average *L* and/or *W* values. In addition, the impact of thermal expansion is a fundamental physical phenomenon with first order influence; this effect causes the mineral grains to swell, with the pore space concomitantly compressed to some extent. This response is examined by the quantitative outputs of machine learning and is shown by the *L* and *W* of a certain pore in sample H1 being smaller at 200 °C than at 100 °C (Fig. 7(a)). Similarly, the selected pore in sample H2 has greater *L* and *W* values at 200 °C than at 300 °C (Fig. 7(b)). In addition, heating dehydrates some of the clay minerals (especially montmorillonite), by illitization, which enables the shrinkage of individual mineral grains and thus enlarges *L* and/or *W* values (Kang et al., 2020). The illitization effect generally occurs at temperatures > 300 °C (He et al., 2022). Therefore, illitization-induced increases in *L* and/or *W* mainly occur at temperatures > 300 °C, which possibly caused the two fiducial pores in Fig. 7 to have final greater *L* and *W* values at 500 °C than at lower temperatures. In general, the variation in pore size, regardless of whether the size increases or decreases, is the combined effect of several factors, in which the relative weighting of each factor at various heating stages still requires to be elucidated.

3.2.2. S value

Based on the sum of pore areas (*S*) (Fig. 8) within the SEM field of view, samples H1 and H2 have a similar cross-sectional 2D porosities of ~1.8%, with sample V1 at ~2.9% at 25 °C – these results from the relatively denser pore distribution in the bedding-perpendicular sample V1 (Fig. 4). This difference further reflects the anisotropic permeability of shales. According to the statistics, the overall sum of areas *S* increases with increasing temperature for all three samples (Fig. 8), indicating that heating effectively generates increased pore space. However, the change in *S* is neither smooth nor monotonic, and comprises two phases, either < 300 °C or > 300 °C (Fig. 8). Similar to the discussion on the influencing factors for lengths *L* and withs *W*, a series of factors jointly affect pore area *S* evolution during heating. Based on Fig. 8, these multiple factors cause fluctuations in the *S* values in a synergistic manner at < 300 °C, while the newly formed pores from the pyrolysis of organic matter and pore space enlargement by illitization-induced grain shrinkage dominate and accumulate pre area *S* at temperatures > 300 °C. This deduction is based on the fact that both organic matter pyrolysis and the illitization occur mainly at temperatures > 300 °C (He et al., 2022; Xu et al., 2022) although this needs to be further verified. As a result, the pore areas *S* of the two selected pores initially decreases and then increases (Fig. 7).

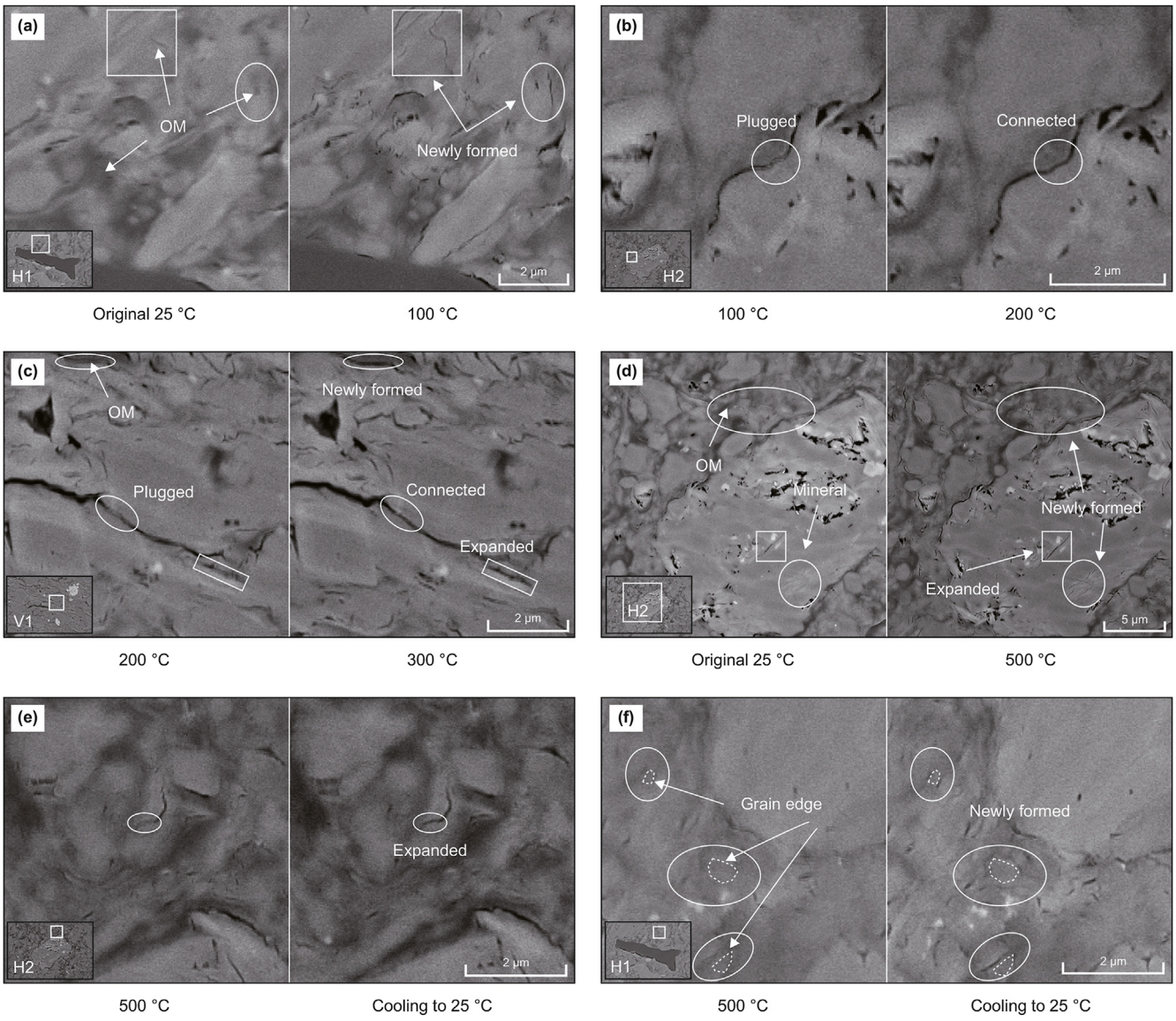

Fig. 5. Evolution of pore structure in low-maturity oil shale during heating. (**a**)–(**d**) Heating phase; (**e**)–(**f**) Cooling phase. OM represents organic matter.

In addition, the heating-induced accumulation of pore number density N (Fig. 4) ensures that the pore area S at higher temperature, as shown in Fig. 9. Accordingly, the component contains more small pores (with inferior S) with the increasing thermal loading bedding-parallel samples H1 and H2; this result is reflected by the leftward deviation of the peak value (Fig. 9(a) and (b)). In contrast, the peak for bedding-perpendicular sample V1 shifts rightward at higher temperatures, indicating that an increase in the number of large pores with heating. This difference also illustrates the trend in anisotropy evident in the evolution of pores in the direction parallel to and perpendicular to bedding.

3.3. Pore orientation characterization

In this work, orientations are not absolute, but relative within the samples —the direction toward the core center is marked as 90° for samples H1 and H2 and vertically upward is treated as 90° for the bedding-perpendicular sample V1 (Fig. 1). The azimuthal orientations θ present at 25 °C are taken as the original azimuths for the collected samples, as shown in Fig. 10, with a wide distribution of azimuths θ ranging from 0° to 180°. With heating, the θ distribution extends outward in concentric semicircles for all the three samples. Visually, bedding-parallel sample H1 (Fig. 10(a)) has a similar trend in azimuthal distribution θ trend to sample H2 (Fig. 10(b)), where minimal pores exist around $\theta = 90°$ during the heating process. In addition, for bedding-perpendicular sample V1, few azimuths θ are distributed in the range of 80°–90°, with this tendency present at all temperatures.

The probability distribution of azimuths θ in Fig. 11 provides a quantitative description of the similar original azimuthal θ distributions for samples H1 and H2. Despite a wide azimuthal distribution, the azimuths θ exhibit two peaks at 30°–60° and 105°–135° for sample H1 (Fig. 11(a)) and sample H2 (Fig. 11(b)). The lines connecting the average and median in the azimuthal distribution θ fluctuate slightly, indicating that heating barely affects the θ distribution. Specifically, the heating-induced pores (including both newly formed and extended pores) are distributed in alignment with the primary pores and little affect the θ distribution in samples H1 and H2. For bedding-perpendicular sample V1, the original azimuthal distribution θ is mainly in the range of

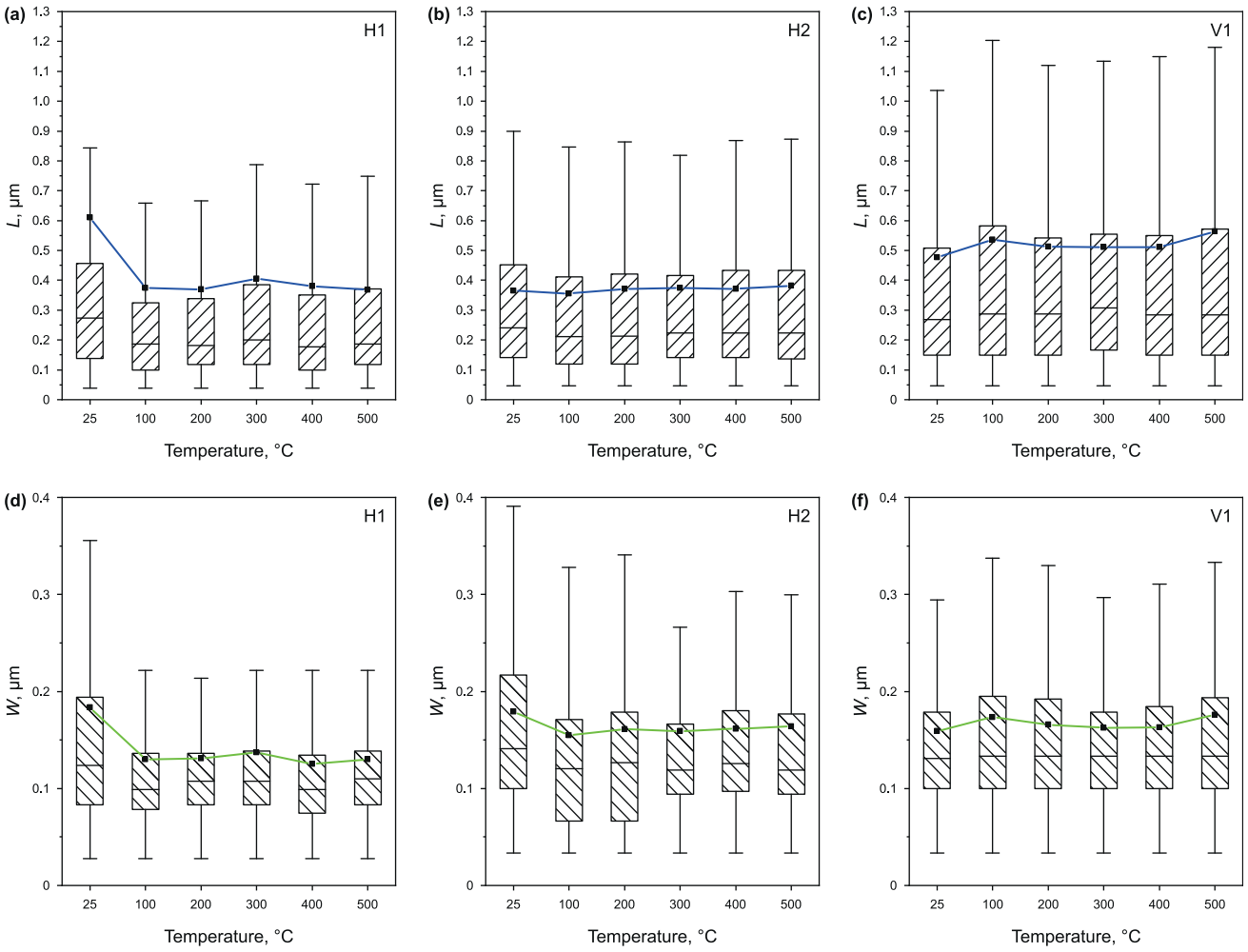

Fig. 6. Statistics of length (*L*) and width (*W*) recovered from machine learning. (**a**)–(**c**) *L* values for SEM images of the three samples; (**d**)–(**f**) *W* values for SEM captures.

120°–100° (Fig. 11(c)) and is invariant with temperature. Similar to samples H1 and H2, the average and median of the azimuthal distribution θ are close for each operating condition, suggesting little influence from heating on the general θ distribution in sample V1. Overall, the θ values demonstrate that heating has little impact on the θ distribution. This trend applies to all three samples and indicates inconspicuous anisotropy with respect to θ evolution during heating.

3.4. Pore shape expression

Pore shape influences fluid transport within tight shales (Song et al., 2018) and thus is of importance in assessing shale reservoir properties. Herein, the parameters of aspect ratio *AR*, roundness and solidity are introduced to quantify the shape of pores with respect to their proximity to a circle and roughness.

Only slight difference exists in the statistics of the *AR* distribution before then after heating —this tendency is apparent for all three samples (Fig. 12). For bedding-parallel samples H1 (Fig. 12(a)) and H2 (Fig. 12(b)), the *AR* values of the pores are mainly distributed in the range of 1–3, and the median *AR* values is ~2 for all operating temperatures. The *AR* distribution of bedding-perpendicular sample V1 is concentrated on the range of 1–4 with a median of ~2 over all temperatures. These results indicate that the elongation of the original pores is not strong, and heating barely changes this.

Roundness is analogous to the inverse of the *AR* value and is used to determine how closely a pore approaches a circle (roundness of 1 represents a circle). The original roundness values for samples H1 and H2 (Fig. 13(a) and (b)) are ~0.5 and ~0.6, respectively, while that for sample V1 is ~0.5 (Fig. 13(c)). Thus, medians and means for roundness are similar, indicated by their synchronous change in Fig. 13. After heating, the average and median of the roundness distribution remain constant at ~0.5. This phenomenon, accompanied with the overall roundness distributions in Fig. 13, indicates that the heating-induced pores (e.g., newly formed pores) have a similar roundness (average of ~0.5) to the original pores and thus minimally perturb the roundness distribution. This statistical trend is isotropic, supported by the comparison between samples H1/H2 and sample V1 (Fig. 13).

Solidity is used to assess the convexity of a pore; a value of 1 correlates to a full-fledged pore, and all other values are less than 1. Derived from the machine learning results, Fig. 14 shows a similar solidity distribution, where the scope of 0.75–0.90 is the primary zone and the medians are mainly located in the range of 0.80–0.85 with respect to samples H1, H2, and V1 (Fig. 14). This phenomenon indicates a relatively robust solidity and further suggests that the induced pores (e.g., newly formed ones) at high temperature follow a solidity similar to the original pores. Analogous to the *AR* and roundness, the evolution in solidity by heating appears to be isotropic, apparent in the probability and statistics analysis (Fig. 14).

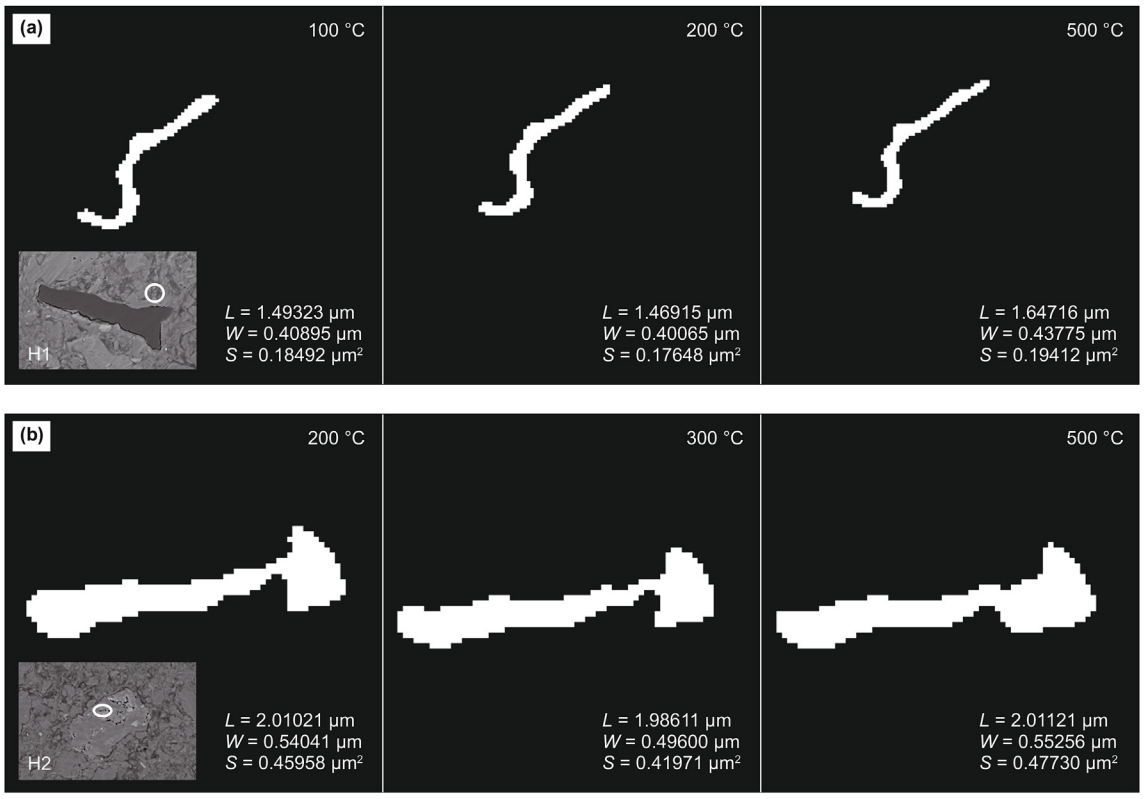

Fig. 7. Evolution of an isolated single pore. (**a**) Sample H1; (**b**) Sample H2.

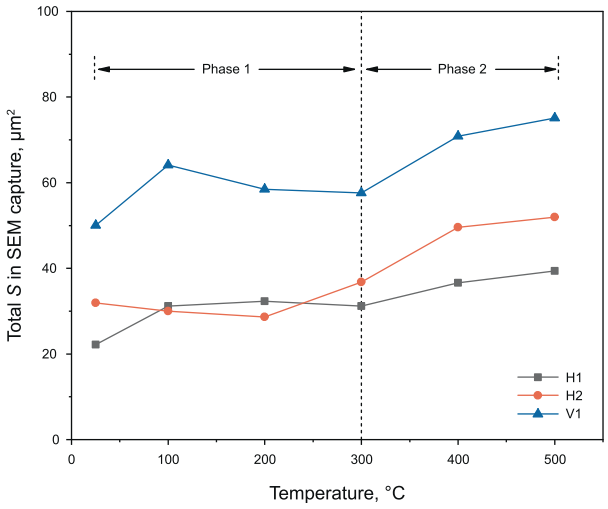

Fig. 8. Total *S* derived from SEM images of the three samples.

3.5. Pore structure evolution model

According to the measurements and statistics recovered by machine learning from the SEM captures, the pore number, size, orientation and shape are quantified. Accordingly, a total of five modes of pore system evolution are observed and detected: 1) formation of new pores, 2) connection of two (or more) pores that were originally disconnected or plugged, 3) extension of pores from original pores, 4) enlargement of pores, and 5) compression of pores (Fig. 15(a)). These evolutions in pore morphology are determined by three principal factors. First, the pyrolysis of organic matter enables new pore space to be formed; second, dehydration (e.g., illitization effect) shrinks the matrix (like mineral grains); and third, heating-induced thermal expansion causes the matrix (like mineral grains) to swell (Fig. 15(b)). By compressing or enlarging pore space, thermal expansion appears to be dominant at < 300 °C, while illitization only becomes prominent at > 300 °C. However, the relative weighting of each influencing factor may be determined and contributing mechanisms constrained at various temperature. Moreover, from the statistical analysis, heating results in changes in *N*, *L*, *W* and *S*, accompanied by evident anisotropic characteristics. In contrast, azimuthal and shape parameters of θ, *AR*, roundness and solidity ds (the probability distribution, average and median) are minimally affected by the high temperature, and exhibit only modest anisotropy.

4. Conclusions

In this work, a series of samples are heated then cooled and concurrently imaged by SEM for a constant field of view. The resulting data are collected and analyzed by a machine learning algorithm. Accordingly, evolution of the quantity, size, orientation and shape of the pores in low-maturity oil shale undergoing thermal upgrading are described in a quantitative manner. The following main conclusions are obtained.

Overall, the number density of pores *N* is increased by heating, with the increase resulting from newly formed pores and potentially countered by a decrease from some disconnected or plugged pores that become connected. The newly formed pores are usually within organic matter but sometimes supplemented by mineral grains, which are speculated to result from the pyrolysis of organic matter and from the matrix shrinkage due to dehydration by illitization.

Heating shortens the average lengths *L* and widths *W* in

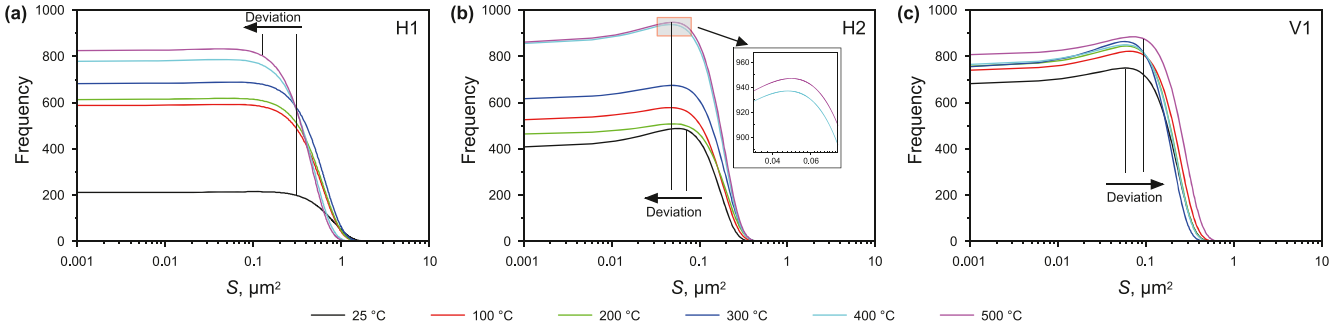

Fig. 9. Distribution of *S* values for three samples. (**a**) Sample H1; (**b**) Sample H2; (**c**) Sample V1.

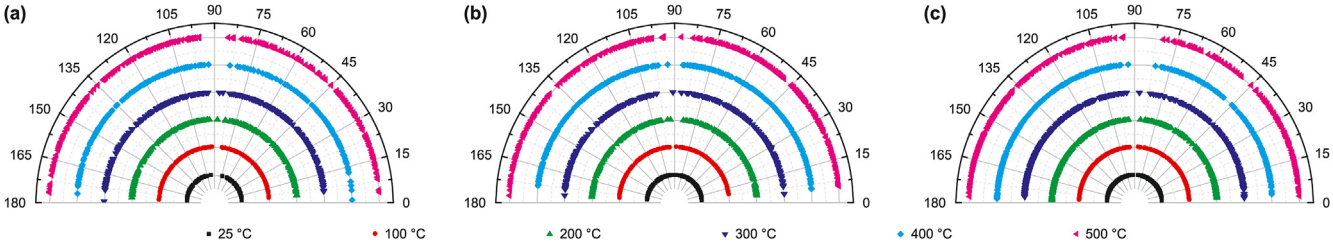

Fig. 10. θ values from the machine learning outputs. (**a**) Sample H1; (**b**) Sample H2; (**c**) Sample V1.

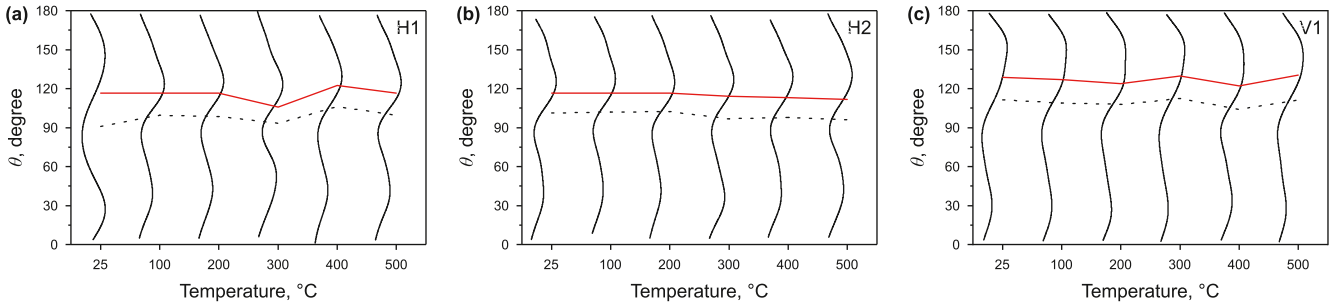

Fig. 11. Probability distribution of pore orientation in SEM captures using kernel smooth fitting. Dashed lines and solid red lines indicate the connecting lines for average and median values at each temperature, respectively. (**a**) Sample H1; (**b**) Sample H2; (**c**) Sample V1.

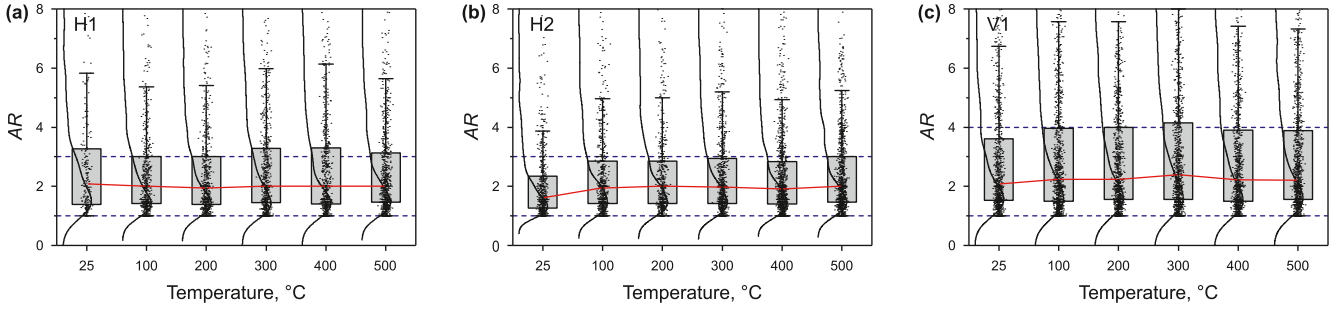

Fig. 12. *AR* values and their distribution using kernel smooth fitting. Red lines are the connecting lines of median values for each temperature. (**a**) Sample H1; (**b**) Sample H2; (**c**) Sample V1.

bedding-parallel samples H1 and H2, indicating that the newly formed pores contain relatively smaller *L* and *W* values than the original pores. The average *L* and *W* values are slightly increased by heating as for bedding-perpendicular sample V1, describing anisotropic evolution in properties; this indicates that the newly formed pores are inclined to have larger *L* and *W* values than protogenetic pores, in the direction perpendicular to shale bedding.

Bedding-perpendicular sample V1 contains a greater pore area *S* and thus has a superior cross-sectional 2D porosity in both pre- and post-heating, relative to bedding-parallel samples H1 and H2. This evolution in area *S* both increases and decreases at < 300 °C but then increases at > 300 °C with increasing temperature. This phenomenon results from the net positive effect of both newly formed pores and dehydration-induced matrix shrinkage, countering the

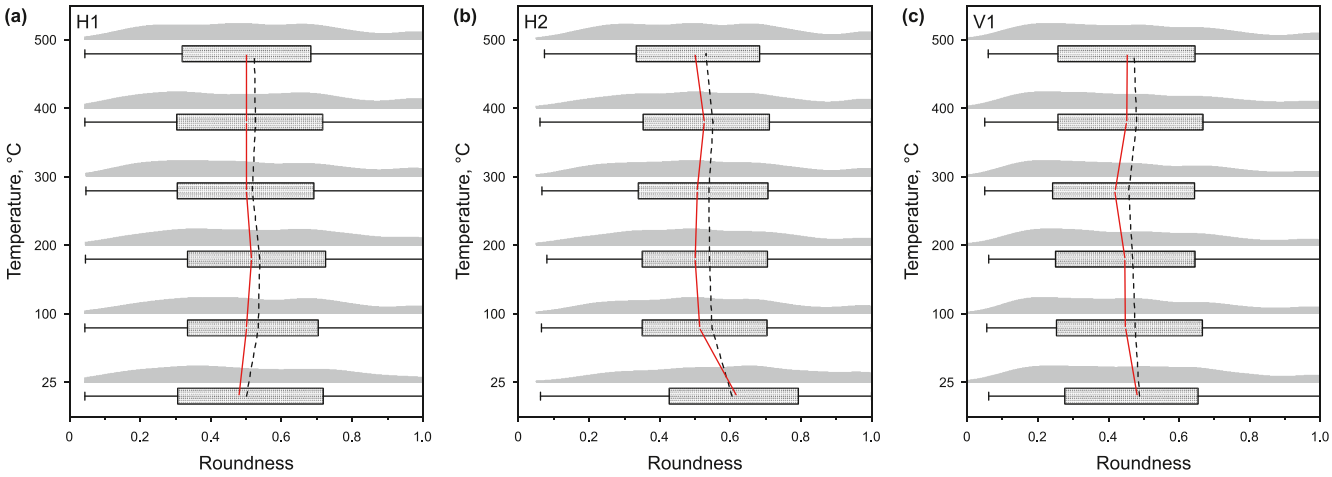

Fig. 13. Frequency plots of pore roundness using kernel smooth fitting. Dashed lines and solid red lines are the connecting lines for average and median values for each temperature, respectively. (**a**) Sample H1; (**b**) Sample H2; (**c**) Sample V1.

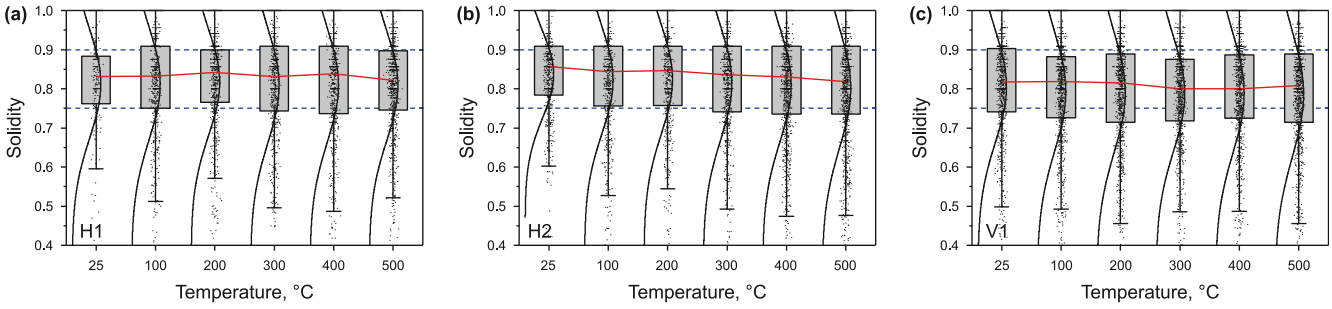

Fig. 14. Normal distribution of solidity for the three samples. Red lines are the connecting lines of median values for each temperature. (**a**) Sample H1; (**b**) Sample H2; (**c**) Sample V1.

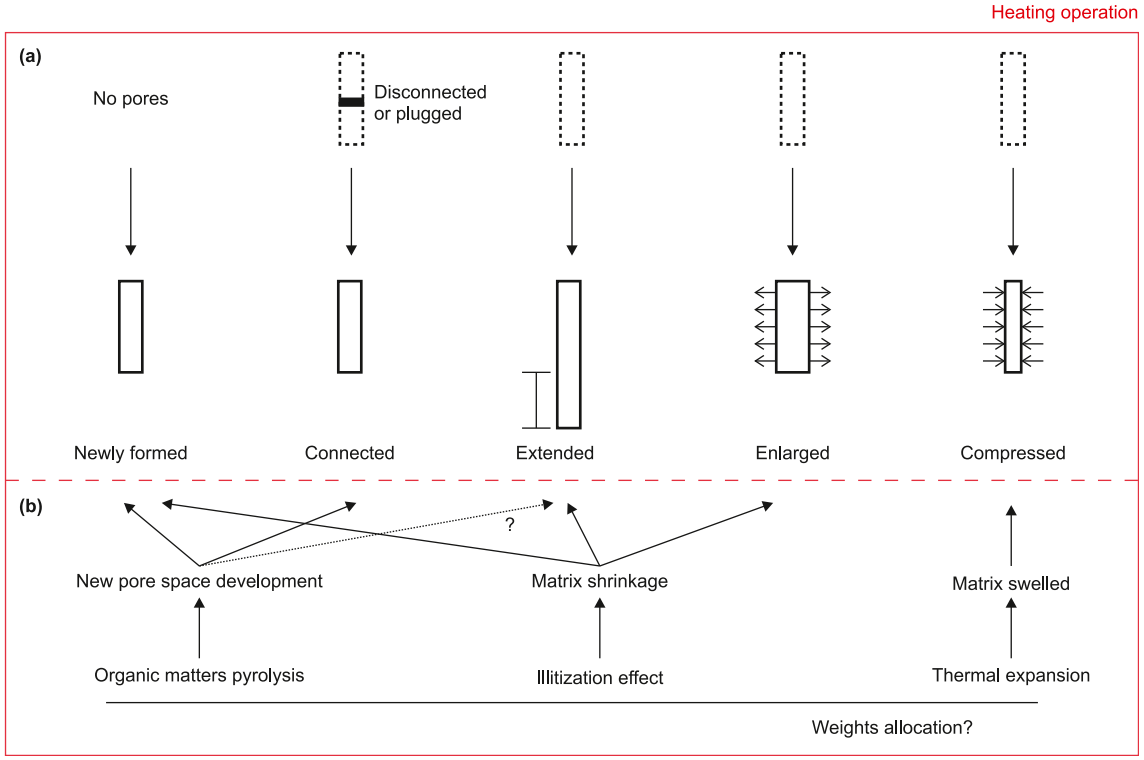

Fig. 15. Pore evolution model during heating in low-maturity oil shales.

negative factors of pore compression by thermal expansion of the shale matrix by heating.

Heating-induced alteration of the pore system in low-maturity oil shale causes few changes in the net orientation of pores nor pore shape; this result is supported by the observation that θ, *AR*, roundness and solidity parameters are statistically invariant. The probability density distributions of θ, *AR*, roundness and solidity are similar both before and after increasing temperature. These results indicate that the impacted pores (e.g., newly formed pores) overall assume the orientation and shape of the original pores. Moreover, a slight anisotropy is associated with the shape of pores in orthogonal sections both parallel and perpendicular to bedding.

Declaration of conflicting interests

The authors declare that the research was conducted in the absence of any commercial or financial relationships that could be construed as a potential conflict of interest.

CRediT authorship contribution statement

Jun Liu: Writing – original draft, Visualization, Supervision, Methodology, Investigation, Funding acquisition, Data curation, Conceptualization. **Xue Bai:** Methodology, Formal analysis, Data curation. **Derek Elsworth:** Writing – review & editing, Methodology.

Acknowledgements

This study was financially supported by the National Key Research and Development Program of China (Grant No. 2022YFE0129800) and the National Natural Science Foundation of China (Grant No. 42202204). Derek Elsworth acknowledges support from the G. Albert Shoemaker endowment.

References

Alfarge, D., Wei, M.Z., Bai, B.J., 2017. Factors affecting CO_2-EOR in shale-oil reservoirs: numerical simulation study and pilot tests. Energy Fuels 31, 8462–8480. https://doi.org/10.1021/acs.energyfuels.7b01623.

Altawati, F., Emadi, H., Pathak, S., 2021. Improving oil recovery of Eagle Ford shale samples using cryogenic and cyclic gas injection methods-An experimental study. Fuel 302, 121170. https://doi.org/10.1016/j.fuel.2021.121170.

Arganda-Carreras, I., Kaynig, V., Rueden, C., Eliceiri, K.W., Schindelin, J., Cardona, A., Sebastian Seung, H., 2017. Trainable Weka Segmentation: a machine learning tool for microscopy pixel classification. Bioimage informatics 33, 2424–2426. https://doi.org/10.1093/bioinformatics/btx180.

Bolotov, A.V., Yuan, C.D., Varfolomeev, M.A., Taura, U.H., Al-Wahaibi, Y.M., Minkhanov, I.F., Derevyanko, V.K., Al-Bahry, S., Joshi, S., Tazeev, A.R., Kadyrov, R.I., Emelianov, D.A., Pu, W.F., Naabi, A., Hasani, M., Al Busaidi, R.S., 2023. In-situ combustion technique for developing fractured low permeable oil shale: experimental evidence for synthetic oil generation and successful propagation of combustion front. Fuel 344, 127995. https://doi.org/10.1016/j.fuel.2023.127995.

Chaudhary, A.S., Ehlig-Economides, C., Wattenbarger, R., 2011. Shale oil production performance from a stimulated reservoir volume. In: SPE Annual Technical Conference and Exhibition. https://doi.org/10.2118/147596-MS.

Comincioli, N., Hagspiel, V., Kort, P.M., Menoncin, F., Miniaci, R., Vergalli, S., 2021. Mothballing in a duopoly: evidence from a (shale) oil market. Energy Economics 104. https://doi.org/10.1016/j.eneco.2021.105583.

Feng, Q.H., Xu, S.Q., Xing, X.D., Zhang, W., Wang, S., 2020. Advances and challenges in shale oil development: a critical review. Advances in Geo-Energy Research 4, 406–418. https://doi.org/10.46690/ager.2020.04.06.

Geng, Y.D., Liang, W.G., Liu, J., Cao, M.T., Kang, Z.Q., 2017. Evolution of pore and fracture structure of oil shale under high temperature and high pressure. Energy Fuels 31, 10404–10413. https://doi.org/10.1021/acs.energyfuels.7b01071.

He, W.Y., Meng, Q.A., Lin, T.F., Wang, R., Liu, X., Ma, S.M., Li, X., Yang, F., Sun, G.X., 2022. Evolution features of in-situ permeability of low-maturity shale with the increasing temperature, Cretaceous Nenjiang Formation, northern Songliao Basin, NE China. Petrol. Explor. Dev. 49, 516–529. https://doi.org/10.1016/S1876-3804(22)60043-0.

Jin, Z.J., Zhu, R.K., Liang, X.P., Shen, Y.Q., 2021. Several issues worthy of attention in current lacustrine shale oil exploration and development. Petrol. Explor. Dev. 48, 1471–1484. https://doi.org/10.1016/S1876-3804(21)60303-8.

Kang, Z.Q., Zhao, Y.S., Yang, D., 2020. Review of oil shale in-situ conversion technology. Appl. Energy 269, 115121. https://doi.org/10.1016/j.apenergy.2020.115121.

Li, L., Hao, Y.M., Lv, Y.T., Wang, C.W., Yao, C.J., Zhao, Q.M., Xiao, P.F., 2020a. Experimental investigation on low-velocity seepage characteristics and influencing factors in a shale oil reservoir. J. Petrol. Sci. Eng. 195, 107732. https://doi.org/10.1016/j.petrol.2020.107732.

Li, X., Cai, J.G., Liu, H.M., Zhu, X.J., Li, Z., Liu, J., 2020b. Characterization of shale pore structure by successive pretreatments and its significance. Fuel 269, 117412. https://doi.org/10.1016/j.fuel.2020.117412.

Lin, T., Liu, X., Zhang, J., Bai, Y., Liu, J., Zhang, Y., Zhao, Y., Cheng, X., Lv, J., Yang, H., 2021. Characterization of multi-component and multi-phase fluids in the Upper Cretaceous oil shale from the Songliao basin (NE China) using T_1–T_2 NMR correlation maps. Petrol. Sci. Technol. 39, 1060–1070. https://doi.org/10.1080/10916466.2021.1990318.

Liu, C., Shi, B., Zhou, J., Tang, C.S., 2011. Quantification and characterization of microporosity by image processing, geometric measurement and statistical methods: application on SEM images of clay materials. Appl. Clay Sci. 54, 97–106. https://doi.org/10.1016/j.clay.2011.07.022.

Liu, J., Xie, L.Z., He, B., Gan, Q., Zhao, P., 2021. Influence of anisotropic and heterogeneous permeability coupled with in-situ stress on CO_2 sequestration with simultaneous enhanced gas recovery in shale: quantitative modeling and case study. Int. J. Greenh. Gas Control 104, 103208. https://doi.org/10.1016/j.ijggc.2020.103208.

Liu, X., Zhang, J., Bai, Y., Zhang, Y., Zhao, Y., Cheng, X., Lv, J., Yang, H., Liu, J., 2020. Pore structure petrophysical characterization of the Upper Cretaceous oil shale from the Songliao Basin (NE China) using low-field NMR. Journal of Spectroscopy. https://doi.org/10.1155/2020/9067684.

Lormand, C., Zellmer, G.F., Németh, K., Kilgour, G., Mead, S., Palmer, A.S., Sakamoto, N., Yurimoto, H., Moebis, A., 2018. Weka trainable segmentation plugin in ImageJ: a semi-automatic tool applied to crystal size distributions of microlites in volcanic rocks. Microsc. Microanal. 24, 667–675. https://doi.org/10.1017/S1431927618015428.

Luo, Z.K., Lin, T.F., Liu, X., Ma, S.M., Li, X., Yang, F., He, B., Liu, J., Zhang, Y., Xie, L.Z., 2023. High-temperature-induced pore system evolution of immature shale with different total organic carbon contents. ACS Omega 8, 12773–12786. https://doi.org/10.1021/acsomega.2c07990.

Pavicic, I., Brisevac, Z., Vrbaski, A., Grgasovic, T., Duic, Z., Sijak, D., Dragicevic, I., 2021. Geometric and fractal characterization of pore systems in the Upper Triassic dolomites based on image processing techniques (example from Zumberak Mts, NW Croatia). Sustainability 13, 7668. https://doi.org/10.3390/su13147668.

Sadiki, A., Kaminsky, W., Halim, H., Bekricet, O., 2003. Fluidised bed pyrolysis of Moroccan oil shales using the hamburg pyrolysis process. J. Anal. Appl. Pyrol. 70, 427–435. https://doi.org/10.1016/S0165-2370(03)00002-0.

Sezer, G.I., Kambiz, R., Bekir, K., Goktepe, A.B., Sezer, A., 2008. Image analysis of sulfate attack on hardened cement paste. Mater. Des. 29, 224–231. https://doi.org/10.1016/j.matdes.2006.12.006.

Shi, J., Ma, Y., Li, S.Y., Zhang, L., 2017. Characteristics of thermal bitumen structure as the pyrolysis intermediate of Longkou oil shale. Energy Fuels 31, 10535–10544. https://doi.org/10.1021/acs.energyfuels.7b01542.

Song, R., Yao, W., Liu, J.J., 2018. Microscopic pore structure characterization and fluids transport visualization of reservoir rock. J. Southwest Pet. Inst. 40, 85–105. https://doi.org/10.11885/j.issn.16745086.2018.07.18.03.

Soroushian, P., Elzafraney, M., 2005. Morphological operations, planar mathematical formulations, and stereological interpretations for automated image analysis of concrete microstructure. Cement Concr. Compos. 27, 823–833. https://doi.org/10.1016/j.cemconcomp.2004.07.008.

Sweeney, J., Burnham, A., 1990. Evaluation of a simple model of vitrinite reflectance based on chemical kinetics. AAPG (Am. Assoc. Pet. Geol.) Bull. 74, 1559–1570. https://doi.org/10.1306/0C9B251F-1710-11D7-8645000102C1865D.

Tan, J.Q., Hu, R.N., Luo, W.B., Ma, Z.L., He, G.M., 2021. Pore evolution of lacustrine organic-rich shales: insights from thermal simulation experiments. Energy Fuels 35, 3079–3094. https://doi.org/10.1021/acs.energyfuels.0c03828.

Vatter, M.H., Van Vactor, S.A., Coburn, T.C., 2022. Price responsiveness of shale oil: a Bakken case study. Nat. Resour. Res. 31, 713–734. https://doi.org/10.1007/s11053-021-09972-9.

Wang, Q., Jiao, G.J., Liu, H.P., Bai, J.R., Li, S.H., 2010. Variation of the pore structure during microwave pyrolysis of oil shale. Oil Shale 27, 135–146. https://doi.org/10.3176/oil.2010.2.04.

Wang, Z.D., Lu, X.S., Li, Q., Sun, Y.H., Wang, Y., Deng, S.H., Guo, W., 2020. Downhole electric heater with high heating efficiency for oil shale exploitation based on a double-shell structure. Energy 211, 118539. https://doi.org/10.1016/j.energy.2020.118539.

Wu, T., Pan, Z.J., Liu, B., Connell, L.D., Sander, R., Fu, X.F., 2021. Laboratory characterization of shale oil storage behavior: a comprehensive review. Energy Fuels 35, 7305–7318. https://doi.org/10.1021/acs.energyfuels.0c04082.

Xu, J.J., Liu, Z.J., Bechtel, A., Meng, Q.T., Sun, P.C., Jia, J.L., Cheng, L.J., Song, Y., 2015. Basin evolution and oil shale deposition during Upper Cretaceous in the Songliao Basin (NE China): implications from sequence stratigraphy and geochemistry. Int. J. Coal Geol. 149, 9–23. https://doi.org/10.1016/j.coal.2015.07.005.

Xu, Y., Lun, Z.M., Pan, Z.J., Wang, H.T., Zhou, X., Zhao, C.P., Zhang, D.F., 2022. Occurrence space and state of shale oil: a review. J. Petrol. Sci. Eng. 211, 110183. https://doi.org/10.1016/j.petrol.2022.110183.

Yang, D., Wang, L., Zhao, Y.S., Kang, Z.Q., 2021. Investigating pilot test of oil shale pyrolysis and oil and gas upgrading by water vapor injection. J. Petrol. Sci. Eng. 196, 108101. https://doi.org/10.1016/j.petrol.2020.108101.

Yu, F.N., Sun, P.C., Zhao, K.A., Ma, L., Tian, X.M., 2020. Experimental constraints on the evolution of organic matter in oil shales during heating: implications for enhanced in situ oil recovery from oil shales. Fuel 261, 116412. https://doi.org/10.1016/j.fuel.2019.116412.

Zhao, J., Yang, D., Kang, Z.Q., Feng, Z.C., 2012. A micro-CT study of changes in the internal structure of Daqing and Yan'an oil shales at high temperatures. Oil Shale 29, 357–367. https://doi.org/10.3176/oil.2012.4.06.

Zhao, P., He, B., Zhang, B., Liu, J., 2022. Porosity of gas shale: is the NMR-based measurement reliable? Petrol. Sci. 19, 509–517. https://doi.org/10.1016/j.petsci.2021.12.013.

Zhou, H., Zeng, S., Zhan, L., Xu, G., Qian, Y., 2018. Modelling and analysis of oil shale refinery process with the indirectly heated moving bed. Carbon Resources Conversion 1, 260–265. https://doi.org/10.1016/B978-0-444-64241-7.50240-8.

Zhou, J.P., Yang, K., Zhou, L., Jiang, Y.D., Xian, X.F., Zhang, C.P., Tian, S.F., Fan, M.L., Lu, Z.H., 2021. Microstructure and mechanical properties alterations in shale treated *via* CO_2/CO_2-water exposure. J. Petrol. Sci. Eng. 196, 108088. https://doi.org/10.1016/j.petrol.2020.108088.

Zhu, J.Y., Yang, Z.Z., Li, X.G., Wang, N.L., Jia, M., 2018. Evaluation of different microwave heating parameters on the pore structure of oil shale samples. Energy Sci. Eng. 6, 797–809. https://doi.org/10.1002/ese3.253.